Jing *et al. Biochar* (2026) 8:11
https://doi.org/10.1007/s42773-025-00525-4

Biochar

ORIGINAL RESEARCH **Open Access**

Cage-like *ulva* biochar confined synthesis of Fe_3O_4/ZnO heterojunction nanoparticles for synergistic adsorption and photocatalytic degradation of PFOA

Hua Jing[1,4], Daoqiong Zheng[1,4*], Hao Du[2,4], Haojia Zhu[2,4], Mengshan Chen[3,4] and Yingtang Zhou[1,4*]

Abstract

Perfluorooctanoic acid (PFOA) has emerged as a new urgent pollutant in aquatic environments due to its high persistence and ecotoxicity. In photocatalytic degradation systems, challenges such as rapid recombination of electron–hole pairs (e^-/h^+), short lifespans of reactive oxygen species (ROS), and insufficient ROS generation hinder the efficient degradation of PFOA. This study presents a novel "scallop cage" architecture, constructed using *Ulva* biochar to create confined spaces that encapsulate the Fe_3O_4/ZnO heterojunction. This approach not only controls the crystal size of the Fe_3O_4/ZnO heterojunction but also confines the degradation reactions to a specific space, significantly shortening the mass transfer distance for ROS and effectively mitigating their rapid deactivation in aqueous-phase degradation processes. Furthermore, the confinement effect enhances the generation of multiple reactive species ($\cdot O_2^-$, $\cdot OH$, $^1O_2$, and h^+). The optimized FZS@UBC-2 composite photocatalyst achieved a PFOA removal efficiency of 97.53%. In practical applications, FZS@UBC-2 efficiently decomposes PFOA in complex aqueous matrices and can be easily recovered using an external magnetic field. This work not only expands the application of algae-derived biochar in advanced oxidation processes but also offers a sustainable strategy for addressing persistent organic pollutants in aquatic environments.

Highlights

- The synthesis of *Ulva* biochar produced a scallop shell-like nanoconfined structure with an ultrahigh specific surface area of 3456.548 m^2/g.
- A significant reduction in grain size fof ZnO from 98.7 nm to 14.6 nm was achieved, as confirmed by XRD and SEM analysis.
- The transfer distance for ROS was shortened, maximizing the avoidance of ROS quenching.
- The nanoconfined spaces promoted the substantial generation of O_2^-,$^1O_2$, and h^+
- The removal efficiency of PFOA reached 97.53%.

Keywords Biochar, Confinement synthesis, Adsorption-photocatalysis synergistic degradation, Emerging contaminants (ECs), Perfluorooctanoic acid (PFOA)

---

*Correspondence:
Daoqiong Zheng
zhengdaoqiong@163.com
Yingtang Zhou
zhouyingtang@zjou.edu.cn
Full list of author information is available at the end of the article

Springer

© The Author(s) 2026. **Open Access** This article is licensed under a Creative Commons Attribution 4.0 International License, which permits use, sharing, adaptation, distribution and reproduction in any medium or format, as long as you give appropriate credit to the original author(s) and the source, provide a link to the Creative Commons licence, and indicate if changes were made. The images or other third party material in this article are included in the article's Creative Commons licence, unless indicated otherwise in a credit line to the material. If material is not included in the article's Creative Commons licence and your intended use is not permitted by statutory regulation or exceeds the permitted use, you will need to obtain permission directly from the copyright holder. To view a copy of this licence, visit http://creativecommons.org/licenses/by/4.0/.

Graphical Abstract

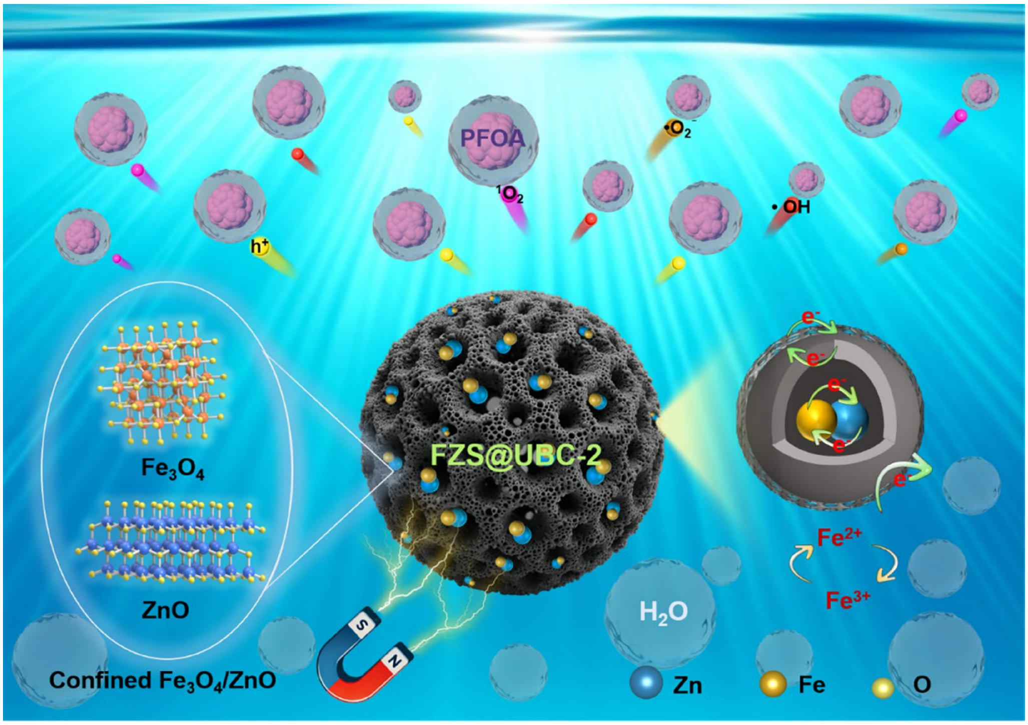

1 Introduction

Perfluorooctanoic acid (PFOA) serves as a prototypical member of per- and polyfluoroalkyl substances (PFAS) (Li et al. 2016a, b), and has been extensively utilized across diverse industries such as medicine, electronics, textiles, and industrial materials since its introduction in the 1940s (Dhore et al. 2021). The widespread anthropogenic application of PFOA has resulted in its pervasive distribution across various environmental compartments, including groundwater, drinking water, sediments, and even remote polar regions (Wee et al. 2023). The compound's significant toxicity and carcinogenic potential (Fenton et al. 2020) have prompted stringent regulatory measures, with the U.S. Environmental Protection Agency (EPA) progressively revising drinking water standards from 70 ng/L in 2016 to a more rigorous 4 ng/L in 2022 (Cotruvo et al. 2020). Alarmingly, current monitoring data reveal that PFOA concentrations in numerous Chinese water bodies substantially exceed these regulatory thresholds (Chen et al. 2016). The environmental persistence of PFOA is primarily attributed to the exceptional stability of the C–F bond (631.5 kJ/mol) and the high electronegativity of fluorine atoms (Tian et al. 2024). Research has shown that PFOA exhibits remarkable resistance to various degradation pathways, including photolysis, adsorption, thermal decomposition, chemical oxidation, microbial action, and metabolic processes (Senevirathna et al. 2024; Hori et al. 2006; Chetverikov et al. 2017). Therefore, it is imperative to identify suitable strategies for the effective removal of PFOA, among which photocatalytic advanced oxidation processes have emerged as particularly promising (Yin et al. 2023, 2025; Yang et al. 2016). Under light irradiation, the photocatalyst generates excited electron–hole pairs (e^-/h^+), which ultimately produce highly reactive oxygen species (ROS) (Malhotra et al. 2024; Rana et al. 2025). ROS are especially effective in breaking the C–F bonds, ultimately degrading PFOA into CO_2 and H_2O (Li et al. 2016a, b). In current research, however, the actual degradation performance of most photocatalysts remains low. The primary factor limiting their activity is the rapid recombination of electron–hole pairs under strong Coulombic interactions, resulting in suboptimal degradation efficiencies (Liu et al. 2022).

Recent advancements in spatial confinement strategies have opened new avenues for enhancing photocatalytic performance. By encapsulating nanophotocatalysts within environments constrained to a certain spatial scale, researchers have achieved notable improvements in various chemical reactions (Tang et al. 2019; Wu et al.

2022; Han et al. 2023). The confinement strategy significantly enhances catalyst performance in two key ways: on the one hand, the physical confinement within support material pores effectively restricts nanoparticle migration while maintaining catalytic activity; on the other hand, constrained crystal growth in nanoscale spaces generates unique structural configurations with increased active sites. Despite these advantages, the field still faces significant challenges, particularly regarding support material selection and practical applicability. Traditional liquid-phase methods have developed several 3D inorganic templates (Yang et al. 2025a, b, c), including mesoporous silica (Liu et al. 2024; Wang et al. 2025), carbon nanotubes (Guo et al. 2021; Yang et al. 2025a, b, c), and zeolites (Grifoni et al. 2021), but these often have limitations such as restricted light penetration, extended diffusion paths, and complex synthesis requirements such as harsh conditions, high costs, and toxic solvents (Zou et al. 2021; Wang et al. 2020; Li et al. 2024). Notably, alternative strategies for assembling confined spaces from any suitable material are also highly valuable. In this context, biochar emerges as a promising alternative confinement substrate material, though its application in photocatalysis remains largely unexplored due to challenges in controlling its typically amorphous structure and pore size distribution. However, recent studies suggest that strategic modification of biochar with appropriate activators can yield hierarchical porous structures with well-defined mesopores, potentially serving as suitable confinement carriers (Ding et al. 2025). The advantages of biochar-based confinement systems are manifold: (1) a large specific surface area with abundant functional groups, (2) excellent photogenerated electron transfer properties, (3) effective nanoparticle dispersion that prevents aggregation, and (4) optimized mass transfer through partial encapsulation and short diffusion channels. These characteristics collectively address critical limitations in nano-photocatalyst applications and enhance practical applications of photocatalytic degradation systems.

Traditional photocatalysts face significant challenges in degrading persistent pollutants such as PFOA: 1) Nanocatalysts are highly prone to aggregation, which reduces active sites and stability; 2) ROS in the aqueous phase are easily deactivated before effectively attacking target pollutants. These limitations severely hinder degradation efficiency and practical application. Therefore, this study presents the design of a novel "scallop cage" photocatalyst, where a photocatalyst carrier and spatial confinement environment are created by regulating the biochar substrate. The biochar substrate can anchor Fe_3O_4 through its active functional groups and electrostatic adsorption. The interaction between the metal and biochar can regulate the electronic states of the metals, while simultaneously altering the active sites of the surrounding carbon materials, thereby firmly anchoring the Nano-ZnO photocatalyst and improving the dispersion of nanoparticles. Additionally, the magnetic properties of Fe_3O_4 facilitate catalyst recovery and recycling. Moreover, by providing a nano-confined space, the mass transfer distance between ROS and pollutants is significantly shortened. Theoretically, this approach satisfies the requirement for spatial confinement of the catalyst while effectively addressing the rapid deactivation of ROS in the aqueous-phase degradation process. This innovative synthesis strategy not only addresses existing challenges in photocatalysis but also opens new avenues for sustainable catalytic applications, especially in environmental remediation of persistent organic pollutants like PFOA.

2 Experimental sections

2.1 Chemical reagents and materials

All chemical reagents, including potassium hydroxide (KOH), zinc acetate dihydrate ($C_4H_6O_4Zn_2H_2O$), ferric chloride hexahydrate ($FeCl_3·6H_2O$), ferrous sulfate heptahydrate ($FeSO_4·7H_2O$), polyvinylpyrrolidone ((C_6H_9NaOH) n, K30), trisodium citrate, dihydrate ($Na_3C_6H_5O_7·2H_2O$), perfluorooctanoic acid (PFOA), and sodium hydroxide (NaOH) were obtained from Sinopharm Chemical Reagent Co., Ltd. All chemicals were of analytical grade and used without further purification. (Other chemicals are provided in the Supporting Information).

2.2 Preparation of FZS@UBC-2

The F@UBC-2 precursor (350 mL) was mixed with 17 mmol $C_4H_6O_4Zn_2H_2O$ and 0.015 g PVP, followed by pH adjustment to 11 using NaOH solution. After hydrothermal treatment at 180 °C for 5 h, the product was washed, dried, and annealed at 600 °C for 2 h under a N_2 atmosphere. Variants $FZ_{0.85}S$@UBC-2 and $FZ_{3.4}S$@UBC-2 were prepared using different zinc precursor concentrations. Nanorod (FZR@UBC-2) and nanoflower (FZF@UBC-2) structures were obtained by modifying the reaction conditions (the preparation of biochar and detailed experimental procedures are provided in the supporting information).

2.3 Degradation experiments

The photocatalytic performance of FZS@UBC-2 was evaluated using a 500 W xenon lamp as the light source. The degradation experiments were conducted in 100 mL of PFOA solution (10 mg/L) containing 0.02 g/L catalyst. After establishing adsorption equilibrium in the dark, photocatalytic degradation was initiated under Xe lamp irradiation. Samples were collected hourly, filtered through 0.22 μm membranes, and analyzed using liquid chromatography-mass spectrometry (LC–MS). The stability of FZS@UBC-2 was assessed through ten consecutive recycling experiments, with XRD analysis performed after each cycle. The effects of pH and common anions (phosphate, chloride, nitrate, bicarbonate, and sulfate) on degradation efficiency were systematically investigated.

2.4 Quantitative analysis of PFOA

The concentration of PFOA during the degradation process was determined using liquid chromatography-mass spectrometry (LC–MS, Agilent 1290 II-6460). The PFOA concentration and intermediates were analyzed under ESI negative ion mode. The liquid chromatography column oven was set to 40 °C. The chromatographic separation was achieved using a C18 column with a mobile phase consisting of 5 mM ammonium acetate (0.1% formic acid) and methanol. The gradient program initiated at 30% methanol, increased to 70% at 4 min, returned to 30% at 7 min, and maintained for 3 min. The flow rate was 0.25 mL/min with a 10 μL injection volume. The defluorination was evaluated using an ion chromatograph (IC, Dionex ICS-5000, USA).

3 Results

3.1 Synthesis and characterization of FZS@UBC

To engineer Ulva biochar as a "scallop cage" nanoreactor carrier framework, this study developed a wall-breaking crushing technique (10-s processing) that enables uniform mixing of biochar with highly hygroscopic KOH activator. In addition, a dual-layer crucible was creatively designed to explore an oxygen-free calcination process by sealing the outer layer. This method outperformed conventional tube furnace calcination techniques, enabling the production of porous biochar with uniform pore distribution and high graphitization (Figure S1). Based on the nano-confinement strategy, magnetic FZS@UBC nanoparticles (Fig. 1a) were subsequently synthesized via a hydrothermal reaction. Meanwhile, as a comparison, Fe_3O_4/ZnO heterojunctions (flower-like and rod-like structures) were synthesized on biochar without confinement treatment by adjusting the reaction conditions (Figure S2). Furthermore, by adjusting the molar ratios of precursors, the optimal photocatalytic activity ratio of Fe_3O_4, ZnO, and biochar was obtained.

3.1.1 Morphology and textural propert

The morphology of FZS@UBC-2 was examined using scanning electron microscopy (SEM) and transmission electron microscopy (TEM) SEM characterization reveals that the Fe_3O_4/ZnO heterojunction was confined and anchored within the pores of the porous carbon (Fig. 1a, b, c). According to the analysis using Image J software, the nanoparticle had a size of 15~17 nm (Fig. 1f), primarily consisting of quasi-spherical nanoparticles, in contrast to the rod-like and flower-like ZnO synthesized without confinement treatment. This confirms that the confinement effect of the porous carbon not only controlled the size of the Fe_3O_4/ZnO heterojunction but also prevented their agglomeration. HRTEM images (Fig. 1e) confirmed crystalline structures with lattice spacings of 0.296 nm (Fe_3O_4 (220)) and 0.260 nm (ZnO (002)), and the existence of biochar could be also observed in the edge region, while EDX mapping (Fig. 1g–k) revealed homogeneous elemental distribution (C, Fe, O, Zn), facilitating the separation of photogenerated e^-/h^+ pairs under illumination and preventing their rapid recombination, which provides a theoretical basis for the efficient photocatalytic degradation performance of FZS@UBC-2.

3.1.2 Chemical compositions characterization analysis

The structure information of the as-prepared samples was analyzed using XRD patterns. The nanocomposite FZS@UBC-2 (Fig. 2a XRD pattern) retained the diffraction peaks of ZnO while exhibiting new peaks corresponding to Fe_3O_4, confirming the successful assembly of the Fe_3O_4/ZnO heterojunction on the porous biochar structure with good crystallinity. The mean crystallite sizes were estimated using the Scherrer equation based on the (311) peak of zinc ferrite, which belonged to the Fd-3 m space group. For FZS@UBC-2, the mean crystallite size was determined to be 24.1 nm. Additionally, the average particle size of S-Nano-ZnO in the FZS@UBC-2 was calculated to be 14.6 nm using Jade software. As shown in Figure S4, the particle size of green-synthesized S-ZnO was calculated to be 98.7 nm using the Debye–Scherrer formula (Edalati et al. 2016). Specifically, the spatial confinement effect of biochar on Nano-ZnO was confirmed by the reduction in particle size, as indicated by the fitting calculations in Jade software. FTIR spectroscopy was employed to analyze the functional groups and structural changes during the confinement of Fe_3O_4/ZnO heterojunctions on *Ulva* biochar. As shown in Fig. 2b, peaks at 2916 and 2853 cm^{-1} are attributed to C-H symmetric stretching vibrations (Xin et al. 2021; Essa et al. 2025), while the band at 1615 cm^{-1} is related to the C=C stretching. However, this peak is absent in the BC spectrum, and the C-H bond at 1439 cm^{-1} suggests the formation of more stable aromatic C=C bonds at higher temperatures. Notably, the C=O group at 1014 cm^{-1} in the ZnO spectrum disappears after loading onto BC, consistent with previous studies (Amir et al. 2025). Furthermore, FZS@UBC-2 exhibited peaks at 1084 cm^{-1} (C=O), 632 cm^{-1} (C–C stretching), 567 cm^{-1} (Fe–O vibration), and 465 cm^{-1} (Zn–O stretching), confirming strong intermolecular interactions between

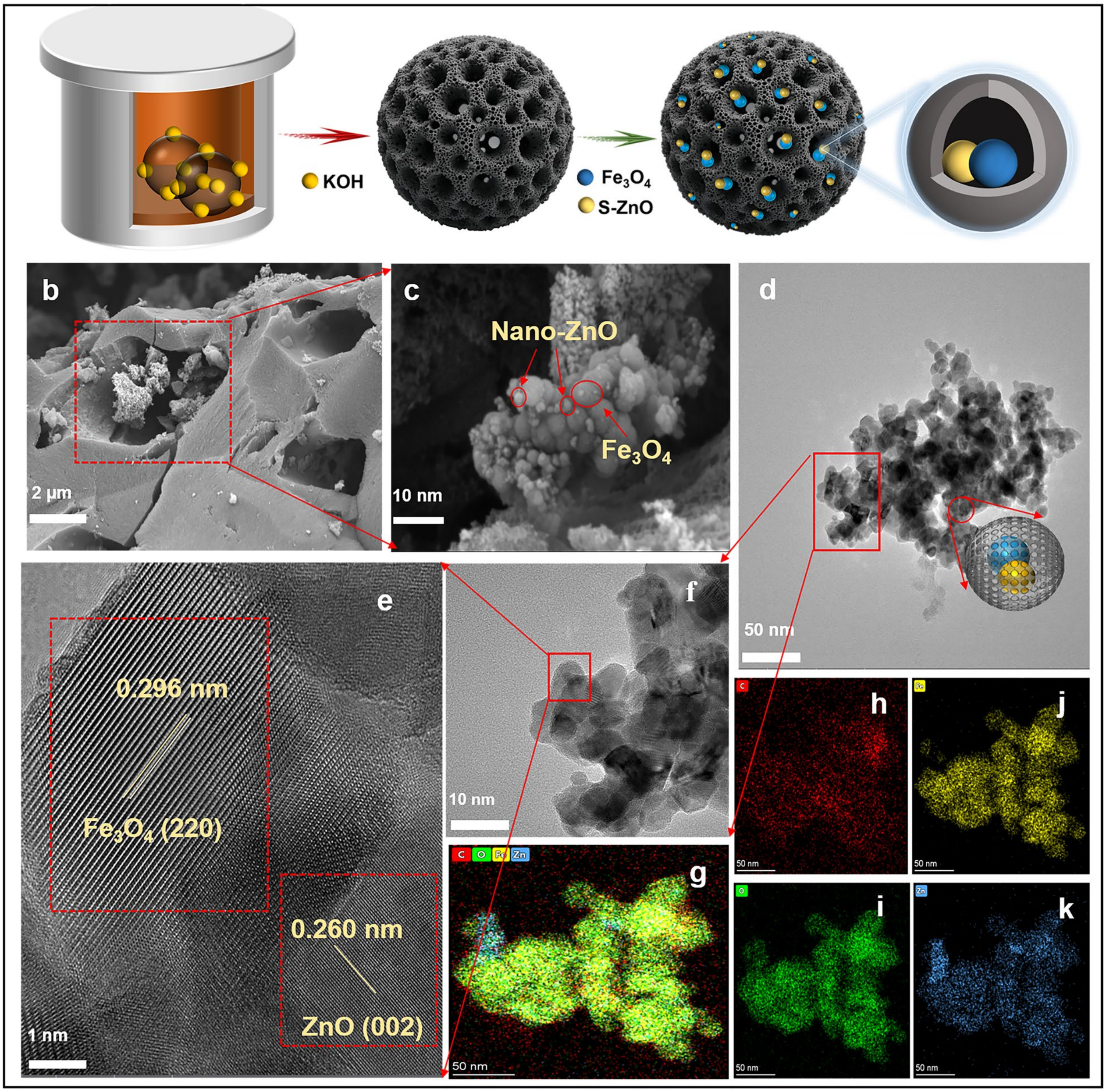

Fig. 1 **a** The schematic diagram of the synthesis process of FZS@UBC-2, **b, c** SEM of FZS@UBC-2, **d, f** TEM of FZS@UBC-2, **e** HRTEM images of FZS@UBC-2, **g** TEM EDS images of FZS@UBC-2, and the corresponding TEM elemental maps of **h** C, **i** O, **j** Fe, **k** Zn

Fe_3O_4/ZnO heterojunctions and the presence of abundant functional groups. To confirm the presence of OVs, EPR measurements were performed. As shown in Fig. 2c, FZS@UBC-2 exhibited stronger Lorentzian intensities and a paramagnetic signal at g = 2.003. It was noteworthy that the EPR signal of FZS@UBC-2 significantly increased after 10 min of light irradiation, indicating the presence of more unpaired electrons delocalized from the π-conjugated network of Fe_3O_4/ZnO molecules, thereby increasing the overall concentration of lone pair electrons. Meanwhile, OVs can act as electron traps, accelerating charge transfer and prolonging carrier lifetimes, which enhances the photocatalytic reaction rates of FZS@UBC-2. Additionally, the hysteresis loop of FZS@S-UBC-2 (Fig. 2d), confirming its ferromagnetic properties, which facilitate material recovery post-degradation and prevent secondary pollution.

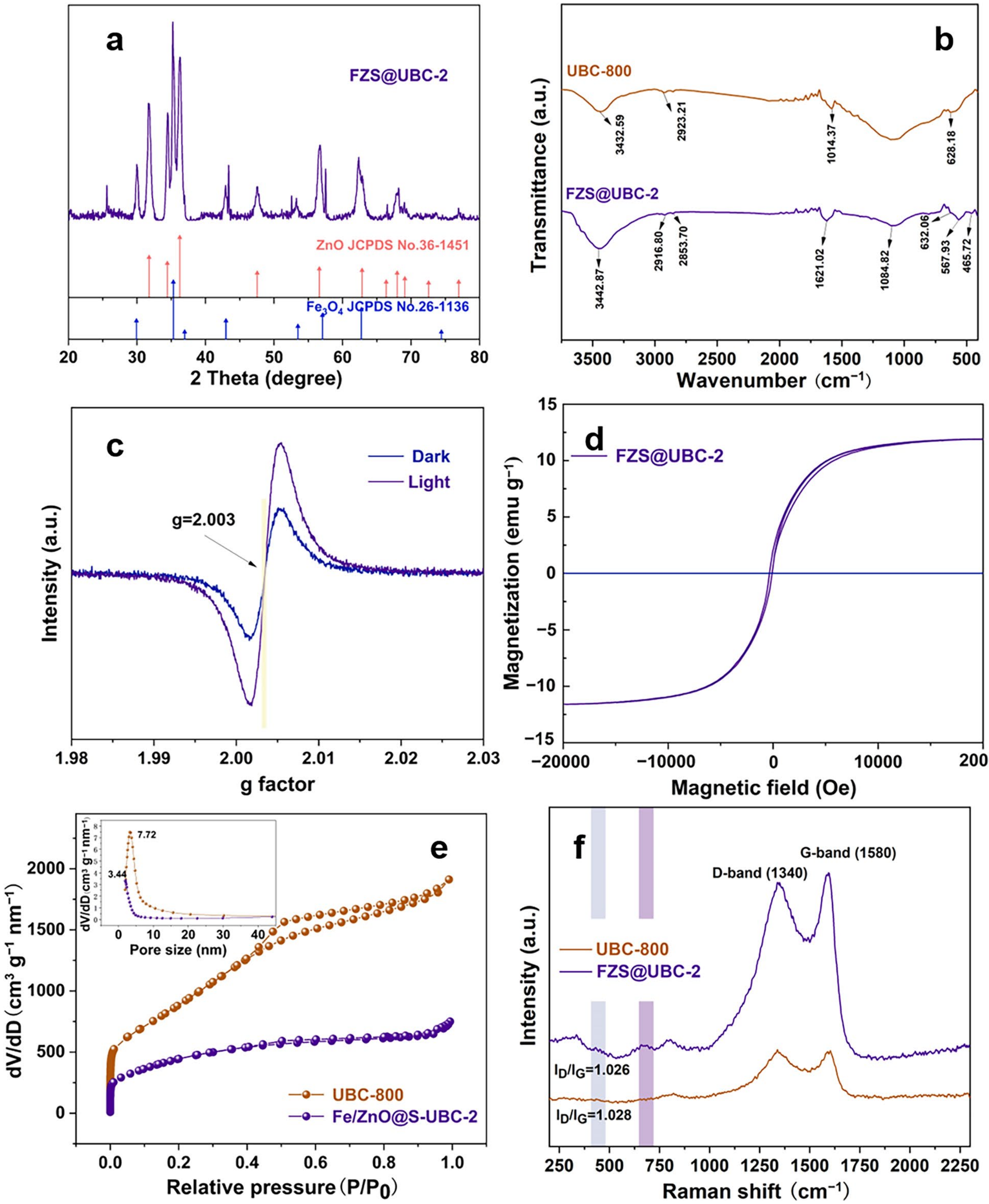

Fig. 2 **a**XRD pattern, **b** N_2 adsorption–desorption isotherm, (inset) pore size distribution, **c** FTIR spectra, **d** Raman spectra, **e** EPR spectra, and **f** magnetization curves

3.1.3 The specific surface area and pore structure analysis

The BET surface area and pore size distribution of the as-prepared samples were analyzed using N_2 adsorption–desorption isotherms and pore-size distribution curves. As shown in Fig. S6, the BC sample exhibited a Type II isotherm according to the IUPAC classification, indicating negligible adsorption capacity, which was consistent with its nonporous structure observed in the SEM images. The BC sample had a surface area of approximately 89.979 m^2/g. In contrast, all other materials displayed typical Type IV isotherms, characterized by an H3 hysteresis loop ($P/P_0 > 0.4$) (Zhu et al. 2018; Wei et al. 2024; Luo et al. 2023), which confirmed their mesoporous structures. The BET surface area of UBC-800 (3456.548 m^2/g) was higher than that of FZS@UBC-2 (1097.658 m^2/g), which was attributed to the blockage of biochar pores by the Fe_3O_4/ZnO heterojunction. Meanwhile, the average pore diameter of FZS@UBC-2 was 3.523 nm, indicating that the heterojunction did not fully fill the carrier, which is beneficial for biochar to play an adsorption role in degradation experiments. Notably, the pore size distribution of FZS@UBC-2 exhibited peaks within the range of 0.4–5 nm, confirming the presence of micropores and small mesopores in the biochar, which facilitates the adsorption of pollutants. However, this does not imply that the confined Fe_3O_4/ZnO heterojunction particle sizes fall within the 0.4–5 nm range. This discrepancy arises because N_2 adsorption is more sensitive to micropore and mesopore configurations, and the complex pore structure of biochar at different scales leads to isotherms indicating smaller pore sizes than those observed in SEM images.

3.1.4 The graphitization degree analysis

The graphitization degree of FZS@UBC-2 was investigated using Raman spectroscopy (Fig. 2f). Two typical characteristic peaks at around 1340 cm^{-1} (D-band, disordered carbon) and 1580 cm^{-1} (G-band, graphitic carbon) were observed. The intensity ratio of the D-band to the G-band (I_D/I_G) reflects the degree of graphitization and defects in carbon-based materials. The I_D/I_G value of FZS@UBC-2 (0.967) confirms a high degree of graphitization, which facilitates the rapid transfer of electrons during photocatalysis (Qu et al. 2022; Velumani et al. 2024; Liu et al. 2014). Additionally, the diffraction peaks observed at 25.615^0 and 43.341^0 in the XRD patterns confirm this (Qiu et al. 2018). Furthermore, peaks at 287 cm^{-1} (Fe), 433–457 cm^{-1} (oxygen vibrations), and 631–702 cm^{-1} (defect states) confirmed the presence of oxygen vacancies, zinc interstitials, or defect complexes, indicating Fe doping-induced changes in ZnO defects.

3.2 Performance analysis of FZS@UBC for PFOA degradation

The degradation performance of FZS@UBC-2 for the removal of PFOA from water was evaluated. As shown in Fig. 3a, with PFOA rapidly degrading due to the synergistic effect of adsorption and photocatalysis in the initial stages, after 4 h of irradiation, the degradation rate reached 97.53%. At the same time, the FZS@UBC-2 photocatalytic system achieved an overall defluorination rate of 27% (Fig. 3b), indicating that the reactive oxygen species (ROS) generated by this system can cleave the highly stable C–F bond. Figure 3c demonstrates that the degradation of PFOA by all catalysts follows a first-order kinetic reaction model, which is a simplified form of the Langmuir–Hinshelwood kinetic model and is widely used to describe the degradation rates of catalysts (Wang et al. 2024; Brindhadevi et al. 2024). Notably, the calculated rate constant (K) for FZS@UBC-2 (0.8285 h^{-1}) during photocatalytic degradation is 33.0 times higher than that of nano-ZnO (0.0251 h^{-1}) and 2.7 times higher than that of Fe@S-UBC-2 (0.3056 h^{-1}) without nano-ZnO doping. Moreover, the degradation rates of FZR@UBC-2 and FZF@UBC-2 reached 67.63% and 50.50%, respectively, suggesting that the morphology of ZnO influences the catalytic activity of the composite materials. In this study, spherical ZnO nanoparticles showed better photocatalytic performance than flower-like and rod-like structures. In addition, the degradation rates of FZR@UBC-2 (rod-like ZnO) and FZF@UBC-2 (flower-like ZnO) without confinement treatment reached 67.63% and 50.50%, respectively. This result further underscores the critical role of the porous biochar structure in creating effective spatial confinement and modifying the nano-ZnO composite photocatalyst, which improves charge carrier transfer efficiency and suppresses the recombination rate of photogenerated electron–hole pairs. FZS@UBC-2 achieved a degradation rate of 54.40% after 1 h of irradiation, significantly higher than the 50.3% observed under dark conditions, confirming the synergistic effect of adsorption and photocatalysis in the degradation process. Additionally, the optimal ratio of the Fe_3O_4/ZnO heterojunction loaded on biochar for photocatalytic degradation was also investigated. The composite catalyst FZS@UBC-2 outperformed $FZ_{0.8}S$@UBC-2 and $FZ_{3.4}S$@UBC-2, likely due to the shielding effect caused by excessive self-aggregation of nano-ZnO, which inhibits photogenerated electron–hole carriers and reduces catalytic activity. A comparison with recent reports on PFOA degradation (Table S1 and Fig. 3d) reveals that the excellent performance of FZS@UBC-2 can be attributed to two key factors: (i) the nano-confinement effect enhances the intrinsic catalytic activity of the Fe_3O_4/ZnO heterojunction by concentrating reactants to accelerate reaction

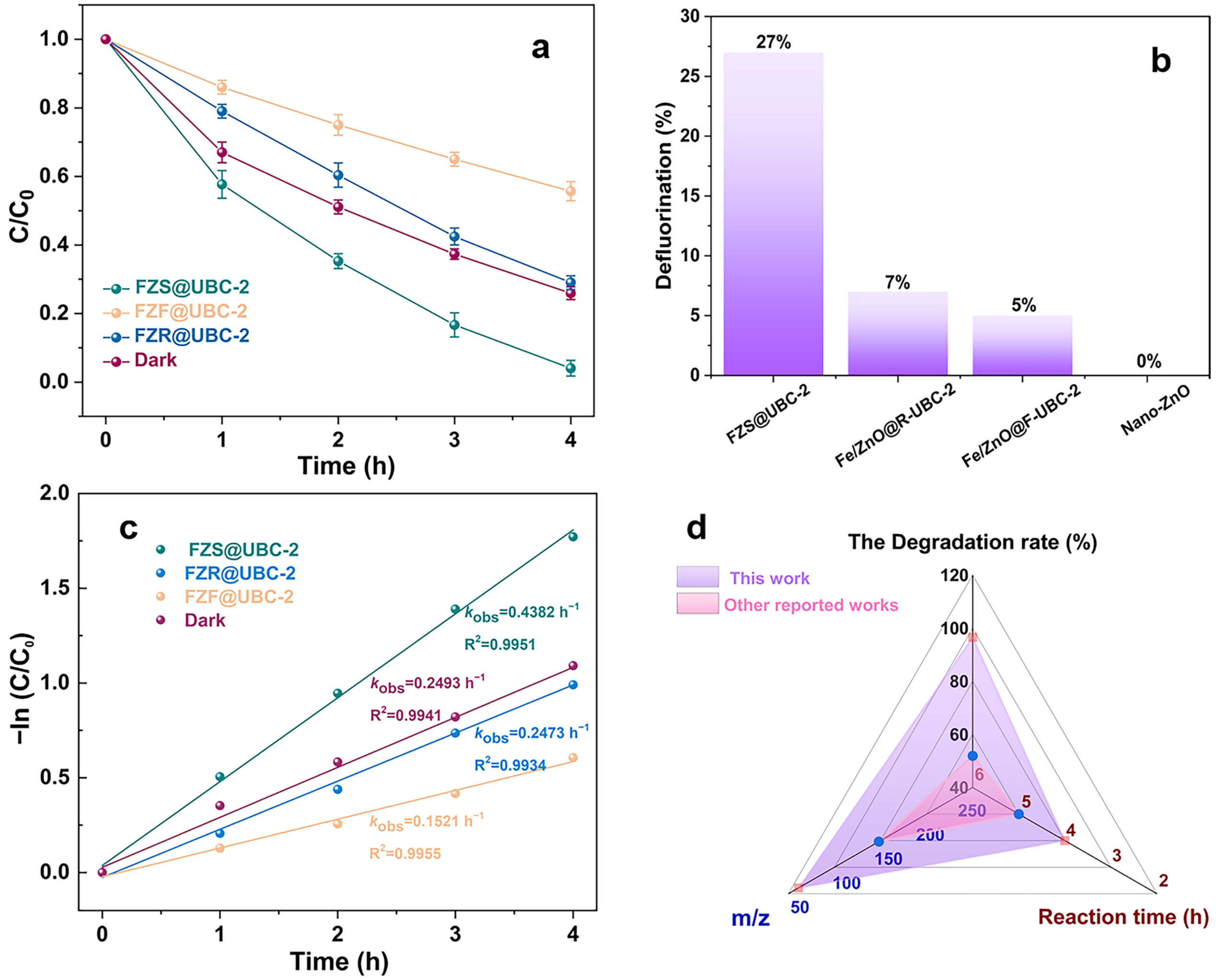

Fig. 3 **a** Photocatalytic degradation of PFOA, **b** defluorination of PFOA, **c** first-order rate constants, and **d** comparison of photocatalytic performance indices with those reported in the literature (as summarized in Table S1)

kinetics, shortening diffusion distances to improve radical utilization efficiency, and preventing radical quenching by excluding competing substances; and (ii) the hierarchical porous biochar not only provides a confined framework but also offers a high surface area with abundant active adsorption and radical reaction sites.

3.3 DFT calculations and possible degradation pathway of PFOA

To explore the degradation mechanism of FZS@UBC-2, the role of reactive species in the degradation system was investigated. As shown in Fig. 4a, the addition of p-benzoquinone, EDTA, and L-tryptophan resulted in a slight decrease in the degradation rate, indicating that $\cdot O_2^-$, h^+ and $^1O_2$ contribute partially to the degradation of PFOA. Notably, the addition of IPA caused the most significant reduction in PFOA degradation efficiency, reaching 67%, underscoring the dominant role of ·OH in the degradation process mediated by FZS@UBC-2. Interestingly, unlike conventional catalysts, the addition of a single radical scavenger did not significantly inhibit PFOA removal, which may be attributed to the strong adsorption capacity of UBC. To further confirm the presence of reactive oxygen species (ROS), electron spin resonance (ESR) spectroscopy with TEMPO and DMPO was employed for characterization (Wang et al. 2022). The results were consistent with the findings of the radical scavenging experiments. In addition, the interfacial electron transfer pathway within the Fe_3O_4/ZnO heterojunction was revealed through density functional theory (DFT) calculations. The Fe_3O_4/ZnO heterojunction exhibits a charge density difference distribution, indicating charge redistribution near the heterojunction interface (Fig. 4g). Furthermore, the driving force behind the Z-scheme

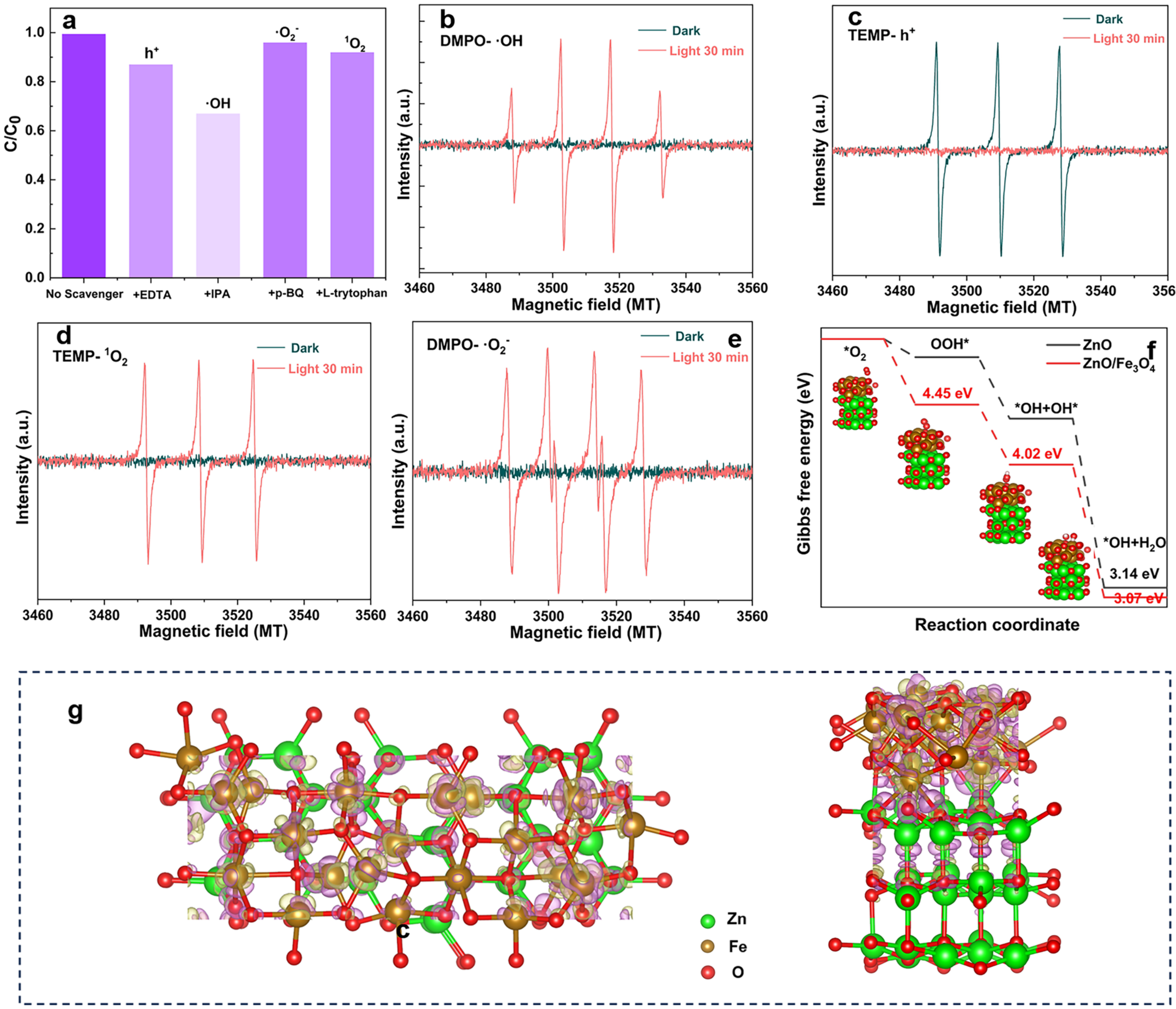

Fig. 4 **a** The influence of scavengers on the PFOA removal efficiency in FZS@UBC-2 system, **b-e** EPR spectrum of FZS@UBC-2: DMPO-·OH, TEMPO-h$^+$, TEMP-·$^1O_2$, DMPO-·O_2^-, **f** Free-energy diagrams, and **g** Charge density isosurface map

mechanism in the Fe_3O_4/ZnO heterojunction can be further elucidated by evaluating the work function (Φ) (Fig. S13).

To gain a deeper understanding of the photocatalytic degradation process and final products of perfluorooctanoic acid (PFOA) in the aqueous phase using the FZS@UBC-2 system, density functional theory (DFT) calculations and LC–MS were employed to analyze the potential degradation pathways. Free radical capture experiments indicated that ·OH plays a significant role in the degradation system, with $^1O_2$, h$^+$, and ·O_2^- also assisting in the degradation. The Fukui index and molecular electrostatic potential (ESP) were used to predict the sites where PFOA is most vulnerable to free radical attack (Fig. 5a-d), leading to the proposal of two potential degradation pathways for PFOA, as shown in Fig. 5e. Pathway I is mainly degraded by chain- shortening (DHEH), involving a four-step process: decarboxylation, hydroxylation, elimination, and hydrolysis. Initially, PFOA undergoes decarboxylation accompanied by defluorination, leading to the formation of intermediate P2 (m/z = 319), which is consistent with DFT results. This intermediate then reacts with ·OH radicals, resulting in further defluorination and the release of F$^-$. Electron spin resonance (ESR) spectroscopy indicates that Fe/ZnO@S-UBC-2 generates ·O_2^- and $^1O_2$ radicals under light irradiation and ultrasonic vibration. Specifically, the P4 molecule is attacked by ·O_2^- and $^1O_2$ radicals, undergoing defluorination and decarboxylation to form P6 (m/z = 113). Subsequently, the $-CF_2-$ group is gradually eliminated under radical

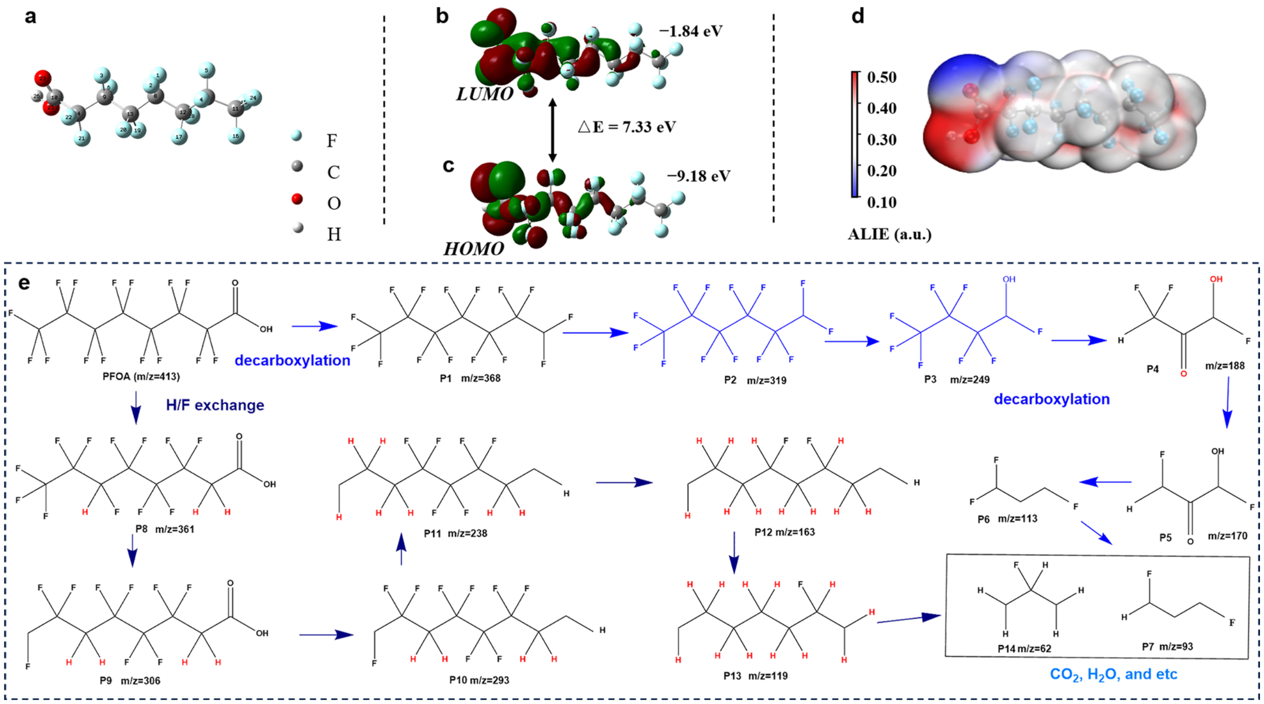

Fig. 5 **a** PFOA molecule structure, **b** LUMO orbital distribution, **c** HOMO orbital distribution, **d** ESP of PFOA, and **e** degradation path way of PFOA

attack. Pathway II involves H/F exchange, producing a series of intermediates, including P8 (m/z = 361) and P9 (m/z = 306), likely through electro-reduction reactions dominated by electrons. The carboxyl group in P9 is attacked by h^+ radicals, leading to further decarboxylation and the formation of P10 (m/z = 293). The F in P10 is subsequently replaced by hydrogen atoms, generating a series of intermediates: P11 (m/z = 238), P12 (m/z = 163), and P13 (m/z = 119). These intermediates undergo further N-demethylation to obtain shorter-chain perfluorocarboxylic acids. Finally, P6 and P13 are further oxidized under radical attack, breaking down into smaller, less toxic molecules such as P7 (m/z = 93) and P14 (m/z = 62). These small molecules ultimately decompose into CO_2 and H_2O, achieving the in-situ green removal of PFOA from water through piezoelectric photocatalysis.

3.4 Optical and carrier transfer properties

3.4.1 Carrier kinetics

To elucidate the generation and transfer mechanisms of electrons (e^-) and holes (h^+), in situ XPS measurements were conducted on FZS@UBC-2 under light irradiation for 30 min. As shown in Fig. 6a, the Fe $2p_3/_2$ spectrum exhibits fitting peaks at 711.1 eV and 713.5 eV, corresponding to Fe (III) and Fe (II), respectively (Jia et al. 2024). The slight increase in binding energy compared to that of Fe (II) confirms the formation of a heterojunction. Additionally, peaks at 724.4 eV are attributed to Fe $2p_1/_2$, characteristic of Fe (II). Satellite peaks at 718.7 eV and 730.4 eV, typical of Fe (III), arise from spin and charge transfer in Fe 2p. The coexistence of Fe (III) and Fe (II) facilitates electron transfer at the catalyst interface. Notably, the content ratio of Fe $2p_1/_2$ decreased from 28.1% to 27.2% after illumination, indicating the participation of both Fe (II) and Fe (III) in the photocatalytic reaction. Furthermore, the peaks of Fe $2p_3/_2$ and Fe $2p_1/_2$ shifted to higher binding energies under light, implying a decrease in the electron density of Fe species and the Fe species acted as an e^- acceptor in the photocatalytic degradation process (Magnier et al. 2024). The C 1 s spectrum of FZS@UBC-2 can be deconvoluted into four components. The main peak at 284.1 eV is attributed to the C–C bond, originating from the biochar formed during calcination. Peaks at 285.9 eV and 287.8 eV correspond to C–O and C = O bonds, respectively, indicating rapid electron transfer during the photocatalytic process. Meanwhile the peak at about 289.8 eV is assigned to C = C and π-π transitions (Shan et al. 2024). The O 1 s spectrum exhibits fitted peaks at 530.3 eV, 531.5 eV, and 532.5 eV, corresponding to lattice oxygen (O_L), oxygen vacancies (O_V), and chemisorbed oxygen (O_C), (Lv et al. 2024). The binding energy of O_V increased by approximately 0.70 eV under light irradiation, indicating that the electron density of O_V decreased under light irradiation. The binding energy of O 1 s increased after irradiated proves that the

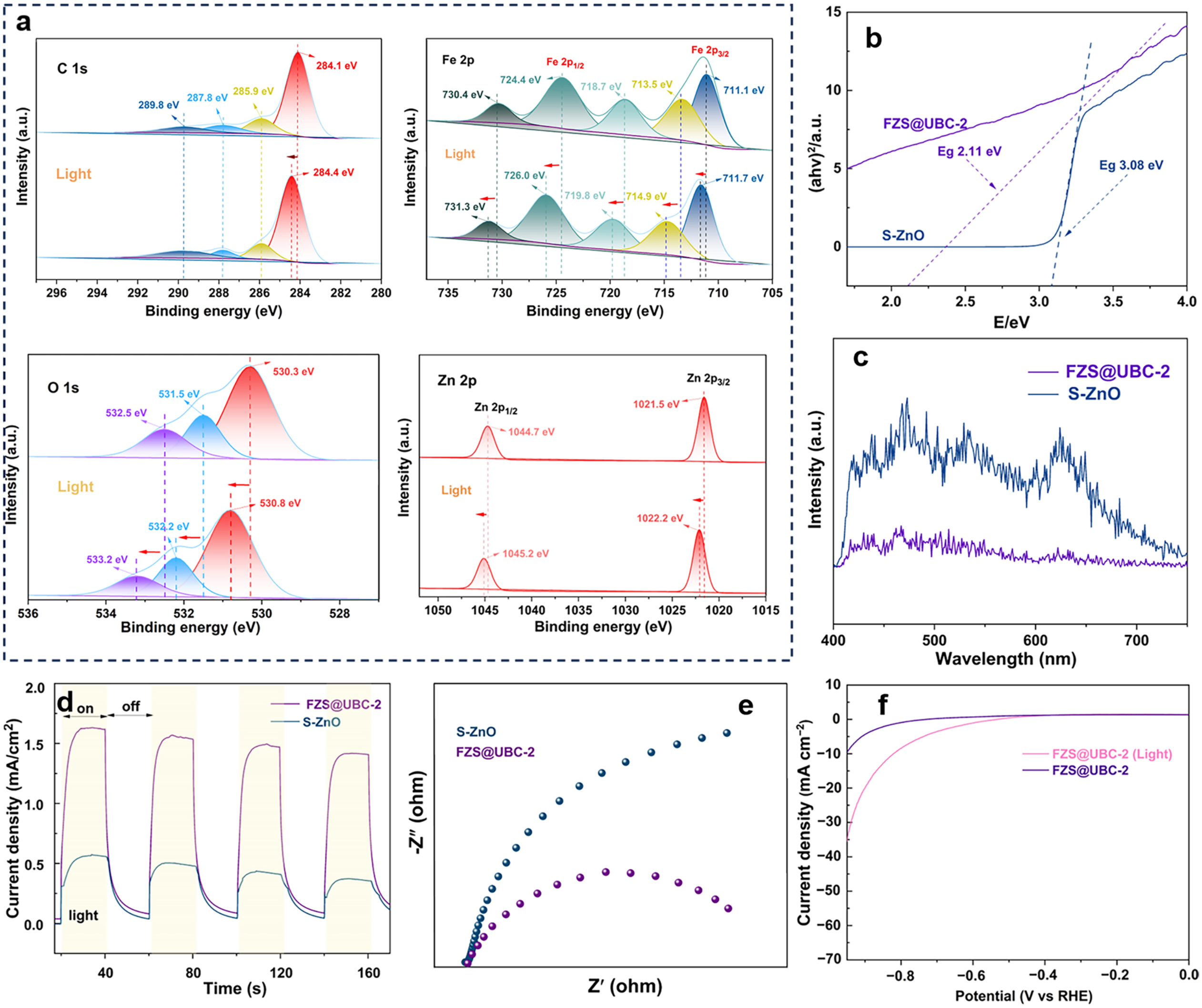

Fig. 6 **a** XPS spectrum, **b** valence band spectra, **c** PL spectra, **d** transient photocurrent responses, **e** EIS Nyquist plots, **f** LSV curves

O played an e^--donating role of the FZS@UBC-2 (Park et al. 2024).

3.4.2 Optical properties

The light absorption capacities of S-ZnO and FZS@UBC-2 are shown in Fig. S9. FZS@UBC-2 exhibited extended absorption into the visible region, indicating efficient visible-light photon absorption. Band gap energies, calculated using Tauc's equation (Fig. 6b) (Bahiraei et al. 2023), were 3.08 eV for S-ZnO and 2.11 eV for FZS@UBC-2. The lower band gap of FZS@UBC-2 facilitates charge carrier (e^-/h^+) transitions, enhancing catalytic performance (Li et al. 2018; Zhang et al. 2022; Chen et al. 2023), attributed to the spatial confinement of the Fe_3O_4/ZnO heterojunction within biochar. The generation of radicals consumes photogenerated charge carriers. To analyze their separation and transfer capabilities, photoluminescence (PL) spectroscopy, electrochemical impedance spectroscopy (EIS), and linear sweep voltammetry (LSV) were performed. The PL spectra (Fig. 6c) revealed a significant decrease in intensity for FZS@UBC-2 compared to S-ZnO. Since PL originates from the recombination of charge carriers (e^-/h^+), the reduction in PL intensity indicates that FZS@UBC-2 can swiftly separate electron–hole pairs while inhibiting charge carrier recombination (Khan et al. 2018). As shown in Fig. 6d, transient photocurrent tests under light irradiation demonstrated that FZS@UBC-2 exhibited a significantly higher current intensity than unmodified nano-ZnO, indicating that the composite catalyst generates more charges under ultrasonic-light synergy. The linear sweep voltammetry (LSV) curves indicated a significant increase in current under illumination (Fig. 6f) (Cai et al. 2021), demonstrating enhanced catalytic activity. The EIS results in Fig. 6e are consistent with the photocurrent results, showing that FZS@UBC-2 has a smaller semicircle radius compared to nano-ZnO, indicating lower charge transfer resistance under light irradiation. This promotes the separation of photogenerated charge carriers. The high conductivity of porous Ulva biochar can be attributed to two factors: (I) the high degree of graphitization of the biochar, as indicated by XRD, and (II) the aromatic structure in Ulva biochar acting as an electron transfer medium, as revealed by FTIR. The biochar loading substantially enhanced the electrical conductivity of FZS@UBC-2, thereby accelerating charge transfer. These results demonstrate that using porous biochar as a confined carrier for the modified photocatalyst significantly improves the separation efficiency of photogenerated electron–hole pairs and enhances electron transfer, thereby increasing the catalytic activity of the composite catalyst.

3.5 Mechanism Analysis

In typical scenarios, electrons in the conduction band (CB) of ZnO tend to transfer to the valence band (VB) of Fe_3O_4 and recombine with the holes in Fe_3O_4. as revealed by Density Functional Theory (DFT) calculations (Figure S13). In this case, the HOMO potential of Fe_3O_4 (+0.4 eV) does not meet the standard oxidation potential of $H_2O/\cdot OH$ (2.4 eV). However, radical scavenging test results indicate that ·OH plays an important role in the degradation of PFOA, suggesting that h^+ in ZnO VB does not transfer to Fe_3O_4 HOMO. This is because, in confined spaces, H_2O_2 locally accumulates, promoting the generation of $^1O_2$, which is associated with the giant exciton effect induced by the confined structure, specifically the Coulomb interaction between electrons and holes (Giant electron–hole interactions in confined layered structures for molecular oxygen activation). Therefore, direct Z-scheme charge transfer between ZnO and Fe_3O_4 is reasonable. Moreover, in situ XPS tests show that under illumination, electrons accumulate on the surface of the composite catalyst, which is consistent with findings reported in other studies regarding Z-scheme heterojunctions. The Z-scheme heterojunction effectively promotes electron transfer and suppresses the recombination of photogenerated charge carriers. Additionally, the residual triplet exciton effect induced by the confined layered space further promotes the generation of $\cdot O_2^-$ and $^1O_2$. Notably, electron transfer induces the Fe (III)/Fe (II) conversion, generating ·OH. At the beginning of degradation, hydrogen bonding, electrostatic interactions, and π-π stacking (as evidenced by XRD, Raman, and XPS analyses) cause pollutant molecules to diffuse and accumulate within the internal microenvironment of the cage-like nanoreactor. Unlike traditional Z-scheme heterostructures, the confinement alters proton and charge transport properties and dynamically redistributes active sites within the catalyst. EPR tests show that h^+ is also an important active species in the photocatalytic degradation process of the composite material, and its production is related to the confined space. Thus, a possible mechanism for photocatalysis is proposed, in which, under illumination, the composite catalyst generates a large number of electrons, and the electron transfer process forms a 3D circulation pathway, where electrons transfer from biochar through C → C, C → Fe/Zn, and Fe/Zn → Fe/Zn to the Fe/Zn nano-heterostructure, with biochar serving as the reaction plane. This creates an internal electric field that accelerates the transfer of electrons and holes, effectively suppressing charge recombination and reducing photo-corrosion. Under photocatalysis, PFOA molecules are immediately attacked by concentrated radicals within the nanoreactor. It has been reported that reactive oxygen species (ROS) do not diffuse efficiently, with 25 nm being the limited diffusion distance for short-lived ROS. Therefore, the scallop cage -like nanoreactor's confined structure shortens the transport distance of ROS and reduces ROS consumption during transfer, maximizing the avoidance of ROS quenching. LC–MS analysis showed the near-complete destruction of organic pollutants. This property, combined with the increased pollutant surface adsorption capacity due to electrostatic interaction as the primary mechanism, synergistically promotes the overall catalytic degradation process under both dark and illuminated conditions.

3.6 Application prospect

To evaluate the adaptability of the system to complex water environments, the effects of common anions and pH on the photocatalytic degradation of PFOA by FZS@UBC-2 were studied. As shown in Fig. 7c, the degradation efficiency of FZS@UBC-2 ranged from 84.80% to 96.53% across a pH range of 2.68 to 10.68, demonstrating excellent photocatalytic properties under varying pH conditions. In natural water bodies, inorganic anions coexist with PFOA and can interfere with the degradation efficiency of the photocatalytic system. Figure 7b reveals that Cl^-, HCO_3^-, HPO_4^{2-}, and SO_4^{2-} exhibited varying degrees of inhibition, with the order of inhibition being $HPO_4^{2-} > SO_4^{2-} > NO_3^- > HCO_3^- > Cl^-$. It is worth noting that HPO_4^{2-} and SO_4^{2-} significantly reduced the degradation efficiency of the system by 17.05% and 12.43%, respectively, primarily due to their ability to trap $\cdot O_2^-$ and $^1O_2$ radicals, converting them into lower oxidation forms. Despite this inhibition, the system still achieved overall degradation rates of 79.48% and 84.10%, which can be attributed to the spatial confinement effect that generated sufficient

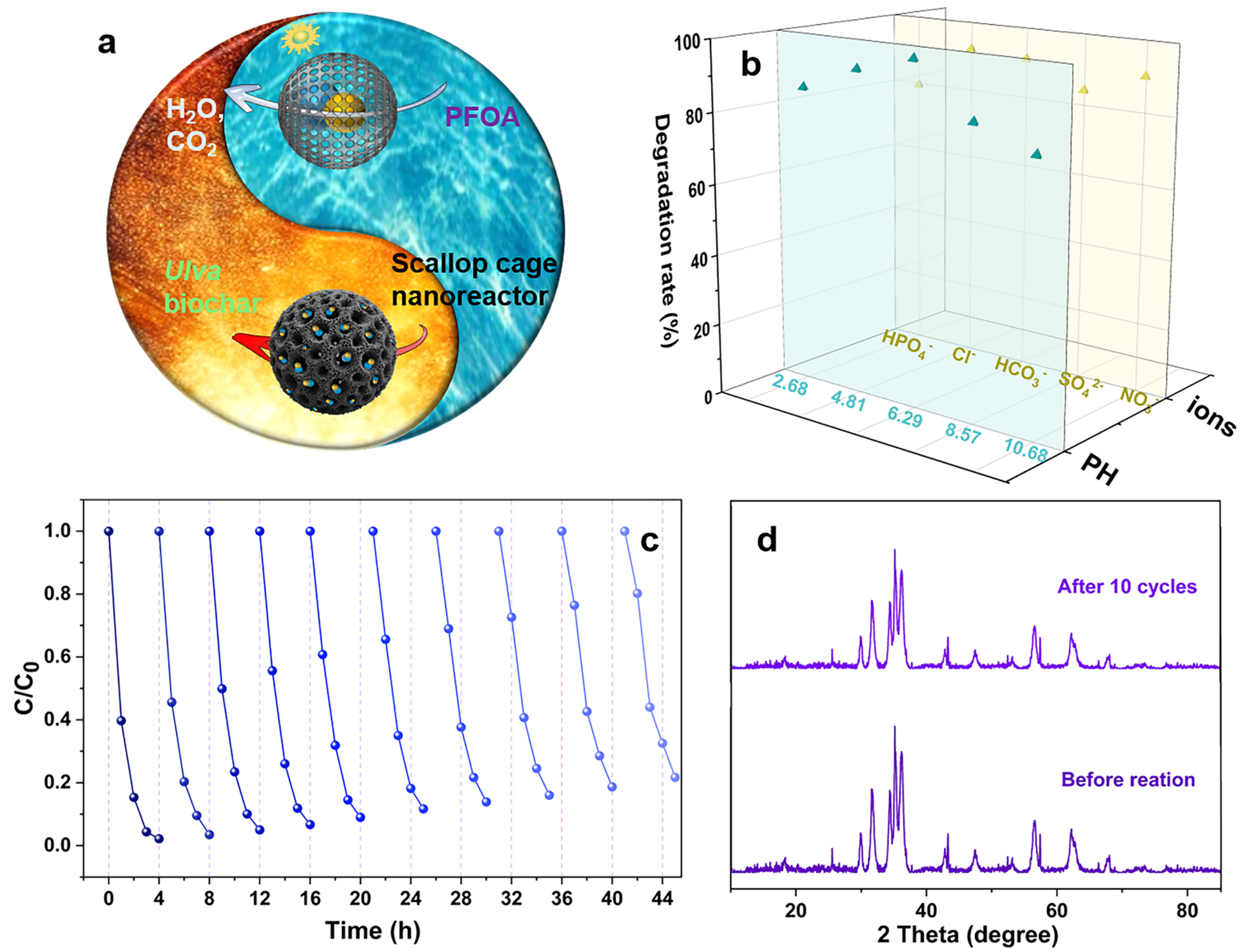

Fig. 7 **a** Schematic representation Fe_3O_4/ZnO heterojunction loaded on an *Ulva* biochar substrate. **b** The effects of pH and different inorganic anions. **c** Recycling tests of FZS@UBC-2. **d** XRD pattern

reactive oxygen species ($\cdot O_2^-$, h^+, $^1O_2$, and $\cdot OH$) and enhanced the local concentration of ROS, reducing the impact of the anions. Additionally, FZS@UBC-2 exhibits excellent adsorption capacity, as indicated by BET and FTIR analyses, allowing the reactants to react more efficiently in the nano-confined space. These results indicate that the system exhibits strong adaptability to complex water environments. The photocatalytic stability of FZS@UBC-2 was evaluated by reusing the catalyst in multiple cycles. As shown in Fig. 8c, after 10 cycles, FZS@UBC-2 maintained a degradation rate of 81.3% for PFOA. XRD analysis of FZS@UBC-2 after 10 cycles (Fig. 7d) confirmed that the crystal structure of FZS@UBC-2 remained unchanged, and FZS@UBC-2 can be easily recovered using an external magnetic field, indicating its great potential for practical applications.

4 Conclusion

In summary, we present an innovative nanoreactor derived from marine biomass *Ulva*, which offers a confined space for the Fe/ZnO heterojunction. This confinement is facilitated by the hierarchical porous biochar (BET) after modification. The porous biochar's confinement effect not only reduces particle size and modifies the crystallization orientation but also prevents aggregation, as confirmed by SEM and TEM analyses. The particle size control of ZnO by the porous biochar was validated using the Debye–Scherrer formula (XRD). In situ XPS measurements revealed the generation and transfer mechanisms of electrons (e^-) and holes (h^+) under light exposure. Raman spectroscopy indicated a high degree of graphitization in FZS@UBC-2, suggesting enhanced electron transfer during photocatalysis. PL, LSV, and transient photocurrent tests demonstrate that, compared to unmodified

ZnO, FZS@UBC-2 generates more electron–hole pairs and promotes their rapid transfer under illumination. Moreover, EIS data showed that FZS@UBC-2 exhibits lower charge transfer resistance. A potential photocatalytic mechanism was proposed based on Tauc equation and density functional theory (DFT) calculations. Notably, EPR tests revealed that, unlike traditional Z-scheme heterojunctions, FZS@UBC-2 generates ·OH and h^+ radicals under light, linked to the giant exciton effect induced by its confined structure. Furthermore, the nanoconfined space reduces the mass transfer distance between the target pollutants and active species, effectively addressing catalyst deactivation caused by the limited diffusion range of active radicals in aqueous systems (typically < 25 nm). Degradation experiments showed that FZS@UBC-2 achieved 97.53% removal efficiency for perfluorooctanoic acid (PFOA), with an apparent rate constant (k) of 0.8285 h^{-1}, along with excellent pH adaptability and stability. These findings highlight the exceptional potential of FZS@UBC-2 as a high-performance photocatalyst for PFOA removal in real-world applications. Our results provide valuable insights into the crucial role of amorphous biochar in the design of 3D porous-channel photocatalysts and pave the way for the practical application of marine biomass-derived photocatalyst carriers in water purification.

Supplementary Information

The online version contains supplementary material available at https://doi.org/10.1007/s42773-025-00525-4.

Supplementary file 1.

Acknowledgements

We would like to express our gratitude to the Hainan Institute of Zhejiang University and the seed funding of Ocean College, Zhejiang University, for their sponsorship.

Author contributions

All authors contributed to the study conception and design. Material preparation, data collection and analysis were performed by Jing Hua. The first draft of the manuscript was written by Jing Hua and Daoqiong Zheng. Resources, writing, reviewing and editing, visualization, supervision, project administration and funding acquisition were carried out by Daoqiong Zheng. Investigation, data curation, software development were done by Yingtang Zhou. Validation, formal analysis, and investigation were performed by Haojia Zhu. Investigation and software development were done by Hao Du. All authors commented on previous versions of the manuscript, read and approved the final manuscript.

Funding

This study was supported by the National Natural Science Foundation of Zhejiang Province (LDT23D06022D06), Key Research and Development Program of Hainan Province (ZDYF2024SHFZ046), the Fundamental Research Funds for the Central Universities (226–2024-00019) and the seed funding of Ocean College (2025LJ001), Zhejiang University.

Data availability

The datasets used or analyzed during the current study are available from the corresponding author on reasonable request.

Declarations

Competing interests

The authors have no relevant financial or non-financial interests to disclose.

Author details

[1]Hainan Institute, Zhejiang University, Sanya 572025, China. [2]Ocean College, Zhejiang University, Zhoushan 310000, Zhejiang, China. [3]Department of Materials Science, Fudan University, Shanghai 200433, China. [4]Zhejiang Key Laboratory of Petrochemical Environmental Pollution Control, National Engineering Research Center for Marine Aquaculture, Marine Science and Technology College, Zhejiang Ocean University, Zhoushan 316004, Zhejiang, China.

Received: 5 April 2025 Revised: 2 September 2025 Accepted: 25 September 2025

Published online: 13 January 2026

References

Amir M, Fazal T, Iqbal J, Din AA, Ahmed A, Ali A, Razzaq A, Ali Z, Rehman MSU, Park YK (2025) Integrated adsorptive and photocatalytic degradation of pharmaceutical micropollutant, ciprofloxacin employing biochar-ZnO composite photocatalysts. J Ind Eng Chem 115:171–182. https://doi.org/10.1016/j.jiec.2022.07.050

Bahiraei H, Azarakhsh S, Ghasemi S (2023) Ternary $CoFe_2O_4$/g-C_3N_4/ZnO heterostructure as an efficient and magnetically separable visible-light photocatalyst: characterization, dye purification, and mechanism. Ceram Int 49:21050–21059. https://doi.org/10.1016/j.ceramint.2023.03.240

Brindhadevi K, Kim TP, Alharbi SA, Ramesh MD, Lee J, Bharathi D (2024) Enhanced photocatalytic degradation of polycyclic aromatic hydrocarbons (PAHs) using NiO nanoparticles. Environ Res 252:118454. https://doi.org/10.1016/j.envres.2024.118454

Cai S, Zhang Q, Wang Z, Hua S, Ding D, Cai T, Zhang R (2021) Pyrrolic N-rich biochar without exogenous nitrogen doping as a functional material for bisphenol A removal: performance and mechanism. Appl Catal B 291:120093. https://doi.org/10.1016/j.apcatb.2021.120093

Chen S, Jiao XC, Gai N, Li XJ, Wang XC, Lu GH, Piao HT, Rao Z, Yang YL (2016) Perfluorinated compounds in soil, surface water, and groundwater from rural areas in Eastern China. Environ Pollut 211:124–131. https://doi.org/10.1016/j.envpol.2015.12.024

Chen L, Wang X, Shi G, Lu G, Wang Y, Xie X, Chen D, Sun J (2023) The regulation of Lewis acid/basic sites in NaFe bimetal MOXs for the controllable photocatalytic degradation of electron-rich/deficient VOCs. Appl Catal B 334:122850. https://doi.org/10.1016/j.apcatb.2023.122850

Chetverikov SP, Sharipov DA, Korshunova TY, Loginov ON (2017) Degradation of perfluorooctanyl sulfonate by strain *pseudomonas plecoglossicida* 2.4-D. Appl Biochem Microbiol 53:533–538. https://doi.org/10.1134/S0003683817050027

Cotruvo JA, Goldhaber SB, Cohen AJ (2020) EPA's unprecedented interim drinking water health advisories for PFOA and PFOS. Ground Water 61:301–303. https://doi.org/10.1111/gwat.13303

Dhore R, Murthy GS (2021) Per/polyfluoroalkyl substances production, applications and environmental impacts. Bioresour Technol 341:125808. https://doi.org/10.1016/j.biortech.2021.125808

Ding S, Wu S, Fang N, Chu Y, Wang P, Ding L (2025) Design and synthesis of porous nano-confined catalysts for VOCs oxidation: a critical review based on pollutant sorts. Sep Purif Technol 352:128158. https://doi.org/10.1016/j.seppur.2024.128158

Edalati K, Shakiba A, Khaki J, Zebarjad S (2016) Low-temperature hydrothermal synthesis of ZnO nanorods: effects of zinc salt concentration, various solvents and alkaline mineralizers. Mater Res Bull 74:374–376. https://doi.org/10.1016/j.materresbull.2015.11.001

Essa RA, El-Aal MA, Sedky A, Zeid EFA, Amin S (2025) *ZnO* NPs-modified biochar derived from banana peels for adsorptive removal of methylene blue from water. J Mol Struct 1321:139821. https://doi.org/10.1016/j.molstruc.2024.139821

Fenton SE, Ducatman A, Boobis A, Dewitt JC, Roberts SM (2020) Per- and polyfluoroalkyl substance toxicity and human health review: current state of knowledge and strategies for informing future research. Environ Toxicol Chem 40:606–630. https://doi.org/10.1002/etc.4890

Grifoni E, Piccini G, Lercher J, Glezakou VA, Rousseau R, Parrinello M (2021) Confinement effects and acid strength in zeolites. Nat Commun 114:2630. https://doi.org/10.1038/s41467-021-22936-0

Guo D, Liu Y, Ji H, Wang CC, Chen B, Shen C, Li F, Wang Y, Lu P, Liu W (2021) Silicate-enhanced heterogeneous flow-through electro-Fenton system using iron oxides under nanoconfinement. Environ Sci Technol 55:4045–4053. https://doi.org/10.1021/acs.est.1c00349

Han J, Guan J (2023) Controllable synthesis of dual-atom catalysts by a confinement-pyrolysis strategy. Chin J Catal 49:1–4. https://doi.org/10.1016/S1872-2067(23)64436-5

Hori H, Nagaoka Y, Yamamoto A, Sano T, Yamashita N (2006) Efficient decomposition of environmentally persistent perfluorooctanesulfonate and related fluorochemicals using zerovalent iron in subcritical water. Environ Sci Technol 40:1049–1054. https://doi.org/10.1021/es0517419

Jia Z, Yang Y, Yang C, Wang D (2024) Magnetic γ-Fe_2O_3/ZnO@CNTs synthesized by a green precipitation method for the degradation of aniline through photocatalysis coupling catalytic ozonation. Appl Surf Sci 659:159866. https://doi.org/10.1016/j.apsusc.2024.159866

Khan I, Qurashi A, Berdiyorov G, Iqbal N, Fuji K, Yamani Z (2018) Single-step strategy for the fabrication of GaON/ZnO nanoarchitectured photoanode their experimental and computational photoelectrochemical water splitting. Nano Energy 44:23–33. https://doi.org/10.1016/j.nanoen.2017.11.050

Li K, Gao P, Xiang P, Zhang X, Cui X, Ma L (2016a) Molecular mechanisms of PFOA-induced toxicity in animals and humans: implications for health risks. Environ Int 99:43–54. https://doi.org/10.1016/j.envint.2016.11.014

Li M, Yu Z, Liu Q, Sun L, Huang W (2016b) Photocatalytic decomposition of perfluorooctanoic acid by noble metallic nanoparticles modified TiO_2. Chem Eng J 286:232–238. https://doi.org/10.1016/j.cej.2015.10.037

Li Y, Li Y, Yin Y, Xia D, Ding H, Ding C, Wu J, Yan Y, Liu Y, Chen N, Wong P, Lu A (2018) Facile synthesis of highly efficient ZnO/$ZnFe_2O_4$ photocatalyst using earth-abundant sphalerite and its visible light photocatalytic activity. Appl Catal B 226:324–336. https://doi.org/10.1016/j.apcatb.2017.12.051

Li S, Zhao Y, Du L, He Y, Wang R, Guo Y, Wang C, Tian T, Wang L, Liu H (2024) Moisture-assisted molecular sieve-confined synthesis of lead-free $CsAgCl_2$ perovskite-derivative nanocrystals. Chem Eng J 482:148966. https://doi.org/10.1016/j.cej.2024.148966

Liu R, Huang H, Li H, Liu Y, Zhong J, Li Y, Zhang S, Kang Z (2014) Metal nanoparticle/carbon quantum dot composite as a photocatalyst for high-efficiency cyclohexane oxidation. ACS Catal 11:328–336. https://doi.org/10.1021/cs400913h

Liu J, Guo C, Wu N, Li C, Qu R, Wang Z, Jin R, Qiao Y, He Z, Lu J, Feng X, Zhang Y, Wang A, Gao J (2022) Efficient photocatalytic degradation of PFOA in N-doped In_2O_3/simulated sunlight irradiation system and its mechanism. Chem Eng J 435:134627. https://doi.org/10.1016/j.cej.2022.134627

Liu H, Shi M, Yang R, Wang Y, Li H, Su Q, Wang T, Wang S (2024) Enhanced photocatalytic hydrogen evolution via yolk–heteroshell TiO_2@TiO_2/SiO_2 nanoreactor with confined Pt nanoparticles. Chem Eng J 499:156118. https://doi.org/10.1016/j.cej.2024.156118

Luo J, Chen Y, Huang H, Ma R, Ma N, Yan F, Xu J, Zhang J, Chen J, Sun S (2023) Microwave-coordinated KOH directionally modulated N/O co-doped porous biochar from *Enteromorpha* and its structure–effect relationships in efficient CO_2 capture. Chem Eng J 473:145279. https://doi.org/10.1016/j.cej.2023.145279

Lv C, Jiao P, Xin H, Wu L, Ouyang G, Hou X (2024) Earth-abundant insulator hydroxyapatite-based composite for full-spectrum photocatalytic degradation of 2, 4- dichlorophenol. Appl Catal B 340:123248. https://doi.org/10.1016/j.apcatb.2023.123248

Magnier L, Cossard G, Martin V, Pascal C, Roche V, Sibert E, Shchedrina I, Bousquet R, Parry V, Chatenet M (2024) Fe–Ni-based alloys as highly active and low-cost oxygen evolution reaction catalyst in alkaline media. Nat Mater 23:252–261. https://doi.org/10.1038/s41563-023-01744-5

Malhotra M, Soni V, Kumar R, Tarannum SP, Thakur S, Le QV, Nguyen LH, Nguyen VH, Raizada P (2024) MOFs-based S-scheme heterojunction photocatalysts: Challenges and prospects to break the selectivity limitation for intensified C_1 products in CO_2 photoreduction. Chem Eng J 506:160238. https://doi.org/10.1016/j.cej.2025.160238

Park SH, Kim S, Park JW, Kim S, Cha W, Lee J (2024) In-situ and wavelength-dependent photocatalytic strain evolution of a single Au nanoparticle on a TiO_2 film. Nat Commun 15:5416. https://doi.org/10.1038/s41467-024-49862-1

Qiu Z, Wang Y, Bi X, Zhou T, Zhou J, Zhao J, Miao Z, Yi W, Fu P, Zhuo S (2018) Biochar-based carbons with hierarchical micro-meso-macro porosity for high rate and long cycle life supercapacitors. J Power Sources 376:82–90. https://doi.org/10.1016/j.jpowsour.2017.11.077

Qu S, Yuan Y, Yang X, Xu H, Mohamed AK, Zhang J, Zhao C, Liu L, Wang B, Wang X, Rinklebe J, Li YC, Wang S (2022) Carbon defects in biochar facilitated nitrogen doping: the significant role of pyridinic nitrogen in peroxymonosulfate activation and ciprofloxacin degradation. Chem Eng J 441:135864. https://doi.org/10.1016/j.cej.2022.135864

Rana P, Soni V, Sharma S, Poonia K, Patial S, Singh P, Selvasembian R, Chaudhary V, Hussain CM, Raizada P (2025) Harnessing nitrogen doped magnetic biochar for efficient antibiotic adsorption and degradation. J Ind Eng Chem 148:174–195. https://doi.org/10.1016/j.jiec.2025.01.025

Senevirathna ST, Tanaka S, Fujii S, Kunacheva C, Harada H, Shivakoti BR, Okamoto R (2024) A comparative study of adsorption of perfluorooctane sulfonate (PFOS) onto granular activated carbon, ion-exchange polymers and non-ion-exchange polymers. Chemosphere 80:647–651. https://doi.org/10.1016/j.chemosphere.2010.04.053

Shan S, Lv Z, Wu HA (2024) Novel readily recyclable Fe3O4/ZnO/loofah biochar composite for efficient degradation of organic pollutants under visible light. Mater Sci Eng B Solid State Mater Adv Appl 303:117272. https://doi.org/10.1016/j.mseb.2024.117272

Tang L, Meng GD, Deng H, Bao H (2019) Confinement Catalysis with 2D Materials for Energy Conversion. Adv Mater 31:1901996. https://doi.org/10.1002/adma.201901996

Tian D, Cheng J, Jia M, Li R, Liu Z, Chen Q (2024) Re-insight of the degradation of perfluorooctanoic acid (PFOA) through three-dimensional rotating gliding arc plasma. Process Saf Environ Prot 194:231–245. https://doi.org/10.1016/j.psep.2024.11.119

Velumani M, Rajamohan S, Pandey A, Pham N, Nguyen V, Hoang A (2024) Nanocomposite from tannery sludge-derived biochar and Zinc oxide nanoparticles for photocatalytic degradation of Bisphenol A toward dual environmental benefits. Sci Total Environ 907:167896. https://doi.org/10.1016/j.scitotenv.2023.167896

Wang JS, Wu K, Yin C, Li K, Huang Y, Ruan J, Feng X, Hu P, Su CY (2020) Cage-confined photocatalysis for wide-scope unusually selective [2 + 2] cycloaddition through visible-light triplet sensitization. Nat Commun 11:4675. https://doi.org/10.1038/s41467-020-18487-5

Wang Y, Peng W, Wang J, Chen G, Li N, Song Y, Cheng Z, Yan B, Hou L, Wang S (2022) Sulfamethoxazole degradation by regulating active sites on distilled spirits lees-derived biochar in a continuous flow fixed bed peroxymonosulfate reactor. Appl Catal B 310:121342. https://doi.org/10.1016/j.apcatb.2022.121342

Wang C, Zhou S, Cui Q, Zhang M, Zheng L, Li S, Liu X, Chen M (2024) Self-floating g-C_3N_4/h-BN/Au photo-thermal catalysts with unprecedented thermostability at solar-activated heating condition for reusable degradation of organic pollutants. Appl Catal B 343:123491. https://doi.org/10.1016/j.apcatb.2023.123491

Wang R, Yin Z, Yang G, Zha Q, Xiong C, Xie Y, Xu J, Luo Y, Hong Z, Xie C, Xue M (2025) Highly efficient multifunctional 3D polyurethane sponge with photothermal responsiveness for efficient oil-water separation and microplastic extraction. Desalination 601:118604. https://doi.org/10.1016/j.desal.2025.118604

Wee SY, Aris AZ (2023) Environmental impacts, exposure pathways, and health effects of PFOA and PFOS. Ecotoxicol Environ Saf 267:115663. https://doi.org/10.1016/j.ecoenv.2023.115663

Wei S, Zhang J, Zhang L, Wang Y, Sun H, Hua X, Guo Z, Dong D (2024) Efficient generation of singlet oxygen for photocatalytic degradation of antibiotics: synergistic effects of Fe spin state reduction and energy transfer. Appl Catal B 358:124406. https://doi.org/10.1016/j.apcatb.2024.124406

Wu Y, Ye C, Yu L, Liu Y, Huang J, Bi J, Xue L, Sun J, Yang J, Zhang W, Wang X, Xiong P, Zhu J (2022) Soft template-directed interlayer confinement synthesis of a Fe-Co dual single-atom catalyst for Zn-air batteries. Energy Storage Mater 45:805–813. https://doi.org/10.1016/j.ensm.2021.12.029

Xin S, Liu G, Ma X, Gong J, Ma B, Yan Q, Chen Q, Ma D, Zhang G, Gao M, Xin Y (2021) High efficiency heterogeneous Fenton-like catalyst biochar modified $CuFeO_2$ for the degradation of tetracycline: economical synthesis, catalytic performance and mechanism. Appl Catal B 280:119386. https://doi.org/10.1016/j.apcatb.2020.119386

Yang G, Yin Z, Han X, Hong Z, Xie C, Ma Y, Xu J, Xue M (2016) Corrugated janus hydrogel-based solar evaporator with enhanced light-trapping nanostructures inspired by corn bracts for efficient seawater desalination. Chem Eng J 512:162459. https://doi.org/10.1016/j.cej.2025.162459

Yang G, Zhang Y, Yin Z, Deng Y, Li Z, Xie Y, Chen Y, Yang C, Yang H, Luo Y, Hong Z, Xue M (2025a) Robust mussel-inspired LBL carbon nanotube-based superhydrophobic polyurethane sponge for efficient oil–water separation utilizing photothermal effect. Fuel 381:133353. https://doi.org/10.1016/j.fuel.2024.133353

Yang G, Yin Z, Zha Q, Wang R, Xie Y, Chen Y, Hong Z, Luo Y, Xue M (2025b) A typha orientalis-inspired 3D Janus solar evaporator with controllable wettability for highly efficient and stable solar desalination. Desalination 595:118318. https://doi.org/10.1016/j.desal.2024.118318

Yang G, Yin Z, Deng Y, Li Z, Chen Y, Xiao W, Hong Z, Luo Y, Xie C, Xue M (2025c) Fabrication of flexible multifunctional graphene-based composite membrane with improved hydrophobicity and thermal conductivity characters for thermal management. Colloids Surf A Physicochem Eng Asp 704:135494. https://doi.org/10.1016/j.colsurfa.2024.135494

Yin Z, Chen X, Chen Z, Song H, Lv P, Xue M, Li H (2023) Superhydrophobic photocatalytic self-cleaning nanocellulose-based strain sensor for full-range human motion monitoring. Adv Mater Interfaces 10(33):2300350. https://doi.org/10.1002/admi.202300350

Yin Z, Yu Q, Chen H, Chen X, Liu K, Li M, Yang X, Chen Y, Xie Y, Luo Y, Xue M (2025) Ce-MOF-based superhydrophobic nancellulose composite membrane with rapid photocatalytic properties and continuous oil-water separation. Int J Biol Macromol 308:142520. https://doi.org/10.1016/j.ijbiomac.2025.142520

Zhang D, Zuo X, Gao W, Huang H, Zhang H, Cong T, Yang S, Zhang J, Pan L (2022) Recyclable ZnO/Fe_3O_4 nanocomposite with piezotronic effect for high performance photocatalysis. Mater Res Bull 148:111677. https://doi.org/10.1016/j.materresbull.2021.111677

Zhu J, Zhu Z, Zhang H, Lu H, Zhang W, Qiu Y, Zhu L, Küppers S (2018) Calcined layered double hydroxides/reduced graphene oxide composites with improved photocatalytic degradation of paracetamol and efficient oxidation-adsorption of As (III). Appl Catal B 225:550–562. https://doi.org/10.1016/j.apcatb.2017.12.003

Zou Y, Xiao K, Qin Q, Shi JW, Heil T, Markushyna Y, Jiang L, Antonietti M, Savateev A (2021) Enhanced organic photocatalysis in confined flow through a carbon nitride nanotube membrane with conversions in the millisecond regime. ACS Nano 15:6551–6561. https://doi.org/10.1021/acsnano.0c09661